

# Time-lapse full-waveform inversion of limited-offset seismic data using a local migration regularization

Espen Birger Raknes<sup>1</sup> and Børge Arntsen<sup>1</sup>

## ABSTRACT

Conventional methods for quantifying time-lapse seismic effects rely on a linear assumption that is easily violated. Therefore, more sophisticated methods are necessary. The full-waveform inversion (FWI) method is an inverse method that is able to reveal time-lapse changes in the image domain, in which the conventional methods break down. We investigated the behavior of FWI using different approaches for applying FWI on limited-offset time-lapse data. We compared acoustic and elastic inversion schemes. We introduced a method for constraining the model update for the monitor model to remove time-lapse artifacts. This method was based on migration of the residuals in the time-lapse data, which, in combination with a local contrast estimation algorithm, formed the update constraint. We found that for limited-offset data, elastic theory was necessary for the success of FWI and that FWI was able to quantify the time-lapse changes in the parameter models. The local migration regularization approach was able to remove time-lapse artifacts.

## INTRODUCTION

Conventional methods for quantifying time-lapse seismic effects in seismic data involve prestack time-migrated data cubes in the migrated image domain (Greaves and Fulp, 1987; Landrø et al., 1999; Lumley et al., 2003). The methods assume that the monitor model can be approximated by a linear perturbation of the baseline model. In cases where production or injection induce strong changes in the rock properties (bulk modulus, densities, and others), the linearity assumption is violated. The migrated data cubes yield images in the time domain, which in cases with complex geology may be inaccurate when converted to depth. Thus, more robust

time-lapse analysis techniques are required to give reliable time-lapse images in these cases.

The full-waveform inversion (FWI) method is a data domain technique for estimating parameters affecting wave propagation using inverse theory (Tarantola, 1984; Mora, 1987; Virieux and Operto, 2009). The inverse problem is nonlinear and ill-posed, which make the problem challenging to solve.

Different approaches exist for applying FWI on time-lapse seismic data (Zheng et al., 2011; Routh et al., 2012). Compared to the conventional time-lapse methods that are basically qualitative methods, the FWI method is able to recover time-lapse effects in elastic parameters directly. Moreover, the method is able to reveal time-lapse changes, in which the linearity assumption for conventional methods is violated.

In a time-lapse setting, where at least two parameter models must be inverted for, the inversions may introduce noise in the time-lapse images that are a direct consequence of the ill-posedness of FWI. We call the noise introduced by the method for time-lapse artifacts. In cases where the true time-lapse effects are small, the time-lapse artifacts may distort the true time-lapse effects, leading to wrong interpretation of the time-lapse images. Therefore, it is important to find inversion approaches that tend to reduce the time-lapse artifacts.

Quei̘er and Singh (2010) use the difference between the inverted baseline and monitor P-wave velocity models to quantify gas saturation changes. Zheng et al. (2011) use ocean bottom cable data to reveal P- and S-wave velocity time-lapse anomalies. In their study, they investigate three different ways of performing time-lapse FWI. The first approach is formed by performing two independent inversions for the baseline and monitor model using the same initial model. In the second approach, they use the inverted baseline model as the starting model for the monitor inversion. The third approach is similar to the second, but in addition, they define the true monitor data set to be the sum of the inverted baseline data set and the difference between the true baseline and monitor data sets. In Routh et al. (2012), synthetic marine time-lapse streamer data are used to

Manuscript received by the Editor 3 October 2013; revised manuscript received 21 January 2014; published online 22 May 2014.

<sup>1</sup>Norwegian University of Science and Technology, Department of Petroleum Engineering and Applied Geophysics, Trondheim, Norway. E-mail: espenn.raknes@ntnu.no; borge.arntsen@ntnu.no.

© 2014 Society of Exploration Geophysicists. All rights reserved.

quantify P-wave velocity anomalies in the subsurface. Raknes et al. (2013) use FWI and the same three approaches as Zheng et al. (2011) on synthetic and real time-lapse data sets to quantify time-lapse effects in the subsurface. FWI is also used for monitoring CO<sub>2</sub> injection considering time-lapse effects in the P-wave velocities using limited-offset data (Zhang et al., 2013).

Limited-offset seismic data contain mainly reflected waves, whereas long-offset seismic data in addition includes other wave phenomena like wide-angle refracted waves, guided waves, mode conversions, and surface waves. For seismic data that are dominated by reflected waves, the acoustic approximation is approximately correct for the kinematics, but not for the amplitudes. The elastic approximation, on the other hand, is correct for the kinematics and the amplitudes. Therefore, if FWI should be applied with success using limited-offset data dominated by reflected waves, an elastic approximation of the wave propagation must be used in the inversion.

In this study, we apply FWI on limited-offset synthetic and real time-lapse data using different time-lapse approaches. In addition, we investigate the difference between acoustic and elastic inversion, in which we use empirical relations to link the inverted P-wave velocities to the density and S-wave velocities. We present a way of creating a gradient constraint that only allows updates in specific areas in the models. The method is based on a migration method in combination with a local contrast detection algorithm. With this approach, it is possible to find areas in the models that are different in the time-lapse data and use this information to constrain the updates in the inversion algorithm, and hence, reduce the amount of time-lapse artifacts. We introduce time-lapse FWI briefly, and describe the local migration regularization (LMR) approach. We investigate the behavior of FWI and the proposed method for creating time-lapse images on a synthetic model using limited-offset data. Then, we apply the approach on a real time-lapse data set. Our investigations show that FWI is able to reveal time-lapse changes. The acoustic-based FWI fails and thus proves that an elastic based FWI is necessary for obtaining reliable results using limited-offset seismic data.

## THEORY

### FWI

The FWI method is an algorithm that iteratively searches for a model that describes given data, by gradually minimizing a given objective function in the data domain. In seismic inverse problems, the objective function is a measure of the dissimilarity between measured data, and data modeled using the current inverted model. The inverse problem is ill-posed resulting in several models giving modeled data that fit the observed data to within the expected noise level. To overcome this problem, a standard procedure is to add penalty terms to the objective function, the purpose of which is to drive the optimization algorithm in a direction that gives a solution closer to the preferred solution (Scales et al., 1990; Virieux and Operto, 2009).

We define the objective function as

$$\Psi(\mathbf{m}) = \Psi_d(\mathbf{m}) + \lambda \Psi_m(\mathbf{m}), \quad (1)$$

where  $\mathbf{m}$  is the model vector,  $\Psi_d(\mathbf{m})$  is the data functional on the data space, and  $\Psi_m(\mathbf{m})$  is the model functional on the model space.

The constant  $\lambda$  is a factor that controls the contributions between the data and model norms. The data norm measures the dissimilarity between the measured and modeled data. The model norm, on the other hand, is interpreted as a regularization term, prior information term, or a combination of the two. Common regularization terms are Tikhonov regularization, which penalizes the roughness of the model, and smoothing regularization, whose purpose is to keep the model smooth. More sophisticated regularization terms may be formed by minimizing the total variation of the model (Virieux and Operto, 2009).

We use a normalized version of the standard least-squares norm as the objective function on the data space. The functional is given as

$$\Psi_d(\mathbf{m}) = \frac{1}{2} \sum_{j=0}^{n_s} \sum_{i=0}^{n_r} \|\hat{\mathbf{u}}_{i,j}(\mathbf{m}) - \hat{\mathbf{d}}_{i,j}\|_2^2, \quad (2)$$

where  $\hat{\mathbf{u}}_{i,j}(\mathbf{m}) = \mathbf{u}_{i,j}(\mathbf{m}) / \|\mathbf{u}_{i,j}(\mathbf{m})\|_2$  is the normalized modeled data,  $\hat{\mathbf{d}}_{i,j} = \mathbf{d}_{i,j} / \|\mathbf{d}_{i,j}\|_2$  is the normalized measured data,  $n_r$  is the number of receivers in the data set, and  $n_s$  is the number of shots in the data set. In what follows, we let  $\mathbf{d}_{i,j} = d_{i,j}(t)$  be the pressure data trace vector. The model functional is defined as

$$\Psi_m(\mathbf{m}) = \frac{1}{2} \|\mathbf{W}(\mathbf{m} - \mathbf{m}_0)\|_2^2, \quad (3)$$

where  $\mathbf{W}$  is some weighting matrix on the model space, whose purpose is to emphasize particular parts of the model vector, and  $\mathbf{m}_0$  is the initial model vector.

Searching for the minimum of  $\Psi(\mathbf{m})$  is done using an iterative minimization algorithm, which in general terms is written as

$$\mathbf{m}_{k+1} = \mathbf{m}_k - \alpha_k \mathbf{H}_k^{-1} \mathbf{g}_k, \quad (4)$$

where  $\alpha_k > 0$  is the step length,  $\mathbf{H}_k^{-1}$  is the inverse Hessian matrix, and  $\mathbf{g}_k$  is the gradient of  $\Psi(\mathbf{m})$  with respect to  $\mathbf{m}$  at step  $k$ . The Hessian matrix involves second-order derivatives of the objective function. Due to the number of unknowns in the inverse problem this matrix is hard to compute. In our implementation, we do not explicitly compute the inverse Hessian matrix. Instead we use the Limited-Broyden, Fletcher, Goldfarb, and Shanno (L-BFGS) algorithm (Nocedal and Wright, 2006), which is a quasi-Newton method that tries to estimate the inverse Hessian matrix using the gradients from previous iterations. The L-BFGS method has proven to be favorable compared to standard conjugate-gradient methods (Brossier et al., 2009).

Taking the derivatives of  $\Psi(\mathbf{m})$  with respect to  $\mathbf{m}$  gives the gradient  $\mathbf{g}$ :

$$\mathbf{g} = \sum_{j=0}^{n_s} \sum_{i=0}^{n_r} \frac{\partial \mathbf{u}_{i,j}(\mathbf{m})}{\partial \mathbf{m}} \hat{\mathbf{r}}_{i,j} + \lambda \mathbf{W}(\mathbf{m} - \mathbf{m}_0), \quad (5)$$

where

$$\hat{\mathbf{r}}_{i,j} = \frac{1}{\|\mathbf{u}_{i,j}\|_2} (\hat{\mathbf{u}}_{i,j} \langle \hat{\mathbf{u}}_{i,j}, \hat{\mathbf{d}}_{i,j} \rangle - \hat{\mathbf{d}}_{i,j}), \quad (6)$$

is the residuals vector. Here,  $\langle \cdot, \cdot \rangle$  is the inner product on the vector space. The first term in equation 5 is calculated using the adjoint-state method, where the residuals  $\hat{\mathbf{r}}_{i,j}$  are reversed in time and

back-propagated from the receiver positions (Tarantola, 1984; Mora, 1987). In our numerical modeling scheme, we use the hyperbolic velocity-stress wave equations (Virieux, 1986), and thus the model gradients must be given in terms of the stress fields. The gradient for the P-wave velocity  $V_p$  is given as (Shipp and Singh, 2002)

$$\nabla_{V_p} \Psi_d(\mathbf{m}) = -\frac{\rho V_p}{2(\lambda + \mu)^2} \sum_{j=0}^{n_s} \int_0^T (\vec{\tau}_{zz} + \vec{\tau}_{xx})(\vec{\tau}_{zz} + \vec{\tau}_{xx}) dt, \quad (7)$$

where  $\lambda$  and  $\mu$  are the Lamé parameters,  $\vec{\tau}_{ii}$  are the forward propagated stresses, and  $\vec{\tau}_{ii}$  are the reverse-time back-propagated stresses.

In theory, it is possible to invert for densities, P-, and S-wave velocities using FWI. However, the three parameters are strongly correlated, and thus inverting for all three parameters increases the amount of unknowns and the ill-posedness of the problem as well. Therefore, we invert for the P-wave velocities and use simple empirical relations to update the densities and S-wave velocities at each iteration in the iterative algorithm. For the S-wave velocity  $V_s$  we use the mudrock line derived in Castagna et al. (1985), which is given as

$$V_s = 0.862V_p - 1172, \quad (8)$$

where  $V_p$  is given in m/s. For the density  $\rho$ , we use Gardner's relation for sedimentary rocks (Gardner et al., 1974):

$$\rho = \begin{cases} 1000 & \text{for } V_p \leq 1500, \\ 310V_p^{0.25} & \text{otherwise,} \end{cases} \quad (9)$$

where the unit for  $\rho$  is kg/m<sup>3</sup>.

The residuals for the normalized least-squares functional 2 differs significantly compared to the residuals for the standard least-squares functional. An important observation is that the residuals in our norm are equal to those that appear if a zero-lag crosscorrelation functional is used (Choi and Alkhalifah, 2012). The reason for this is that the crosscorrelation and our normalized least-squares functional theoretically are the same (up to a constant value).

When seismic data are acquired the amplitudes between each trace may be different due to, for instance, badly calibrated receivers. The benefit of using a normalized functional is the fact that amplitudes are scaled within the objective function, and thus no scaling of the data are necessary beforehand the inversion.

The success of FWI is dependent on the initial model due to the highly nonlinear behavior of the inverse problem, and the local

optimization algorithm. Conventional methods for building initial models are reflection tomography, migration-based velocity analysis, first-arrival traveltimes tomography, and others (Virieux and Operto, 2009). Recently, Weibull et al. (2012) suggest to use wave-equation-migration velocity analysis (WEMVA) to build reliable initial models for FWI. During the initial tests of our implementations, this approach has proven to provide good results.

## Time-lapse full-waveform inversion

We investigate three approaches for time-lapse full-waveform inversion (TLFWI). We denote the data set from the baseline as  $\mathbf{d}_{base}$ , and the monitor data sets as  $\mathbf{d}_{mon}$ . We assume that the receiver and shot positions are equal in the data sets, and that the source signatures are equal between the surveys. In this sense, we assume that the repeatability is good between the data sets.

The first approach for TLFWI is formed by doing two independent inversions using  $\mathbf{d}_{base}$  and  $\mathbf{d}_{mon}$ . The initial model for the two inversions is the same, so all changes are due to the difference in the data sets. To reveal the changes in the models, the difference between two inverted models are computed (see Figure 1a). We call this scheme "approach 1" in what follows.

If we assume that the changes in the subsurface between the acquisitions of the two data sets are small and local, then the inverted model from the inversion of  $\mathbf{d}_{base}$  should be relatively close to the expected inverted model using  $\mathbf{d}_{mon}$ . Thus, using the inverted model for  $\mathbf{d}_{base}$  as the initial model for the inversion using  $\mathbf{d}_{base}$  should give bigger chances for success. This is of course only valid if the base inversions have converged to a reliable solution. In the end, the two models are compared (see Figure 1b). In what follows, we call this scheme "approach 2."

The third approach is an extension of approach 2, where the true monitor data set, in addition, is modified as follows (Zheng et al., 2011)

$$\hat{\mathbf{d}}_{mon} = \mathbf{d}_{base}^i + (\mathbf{d}_{mon} - \mathbf{d}_{base}), \quad (10)$$

where  $\mathbf{d}_{base}^i$  is the inverted baseline data set. By performing this modification, the potential time-lapse artifacts introduced by the inversions are reduced, due to the fact that they are included in  $\mathbf{d}_{base}^i$ . The time-lapse image is created by considering the difference between the inverted models (see Figure 1c). This scheme is called "approach 3" in what follows.

## Local migration regularization

LMR is an extension of approach 2. The purpose of LMR is to remove artifacts in the time-lapse images by constraining the model

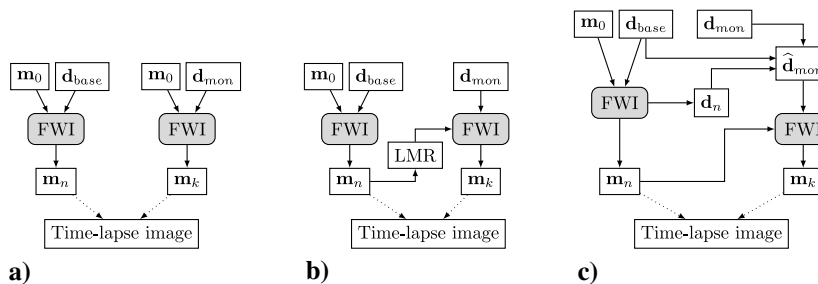


Figure 1. Workflow for TLFWI. (a) Approach 1, (b) approach 2, and (c) approach 3.

updates locally in the models. The idea is to compute the residuals of  $\mathbf{d}_{\text{base}}$  and  $\mathbf{d}_{\text{mon}}$ , and migrate the residuals using the inverted model for the baseline. To create the constraint for the model update, we suggest to use a contrast detection algorithm in combination with a threshold limit.

Assume that the inversion of  $\mathbf{d}_{\text{base}}$  has converged and a final model  $\mathbf{m}_{\text{base}}$  has been obtained. We assume, in addition, perfect repeatability between the baseline data set  $\mathbf{d}_{\text{base}}$  and the monitor data set  $\mathbf{d}_{\text{mon}}$ . The residuals  $\mathbf{r}$  of the two data sets, computed using equation 6, contain only data due to the changes in the subsurface. Running a migration of the residuals using the inverted model  $\mathbf{m}_{\text{base}}$ , results in an image containing information about where the changes in the subsurface occurred.

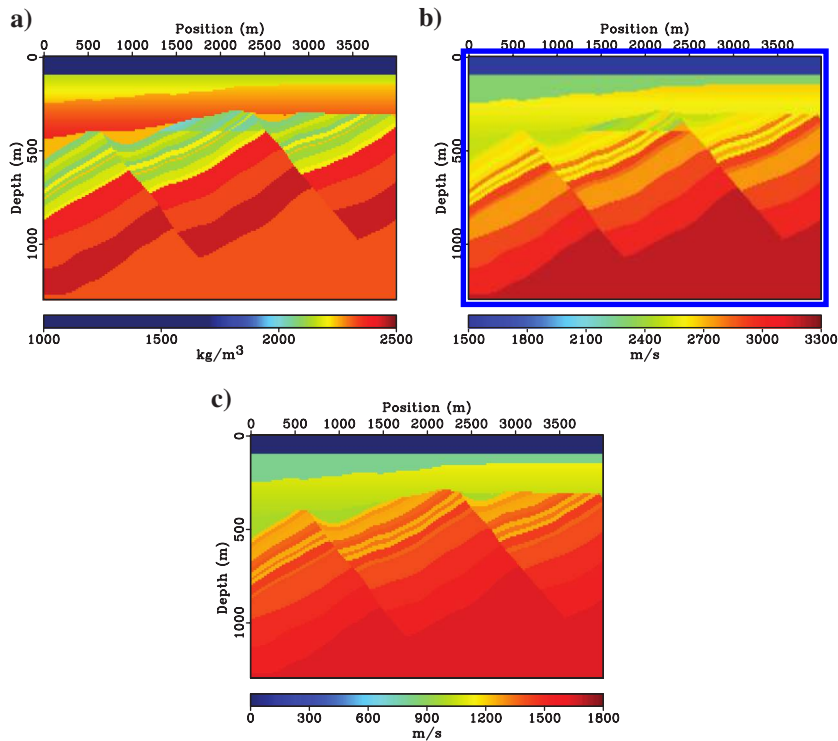


Figure 2. The synthetic model of the Gullfaks field. (a) Density  $\rho$ , (b)  $V_p$ , and (c)  $V_s$ .

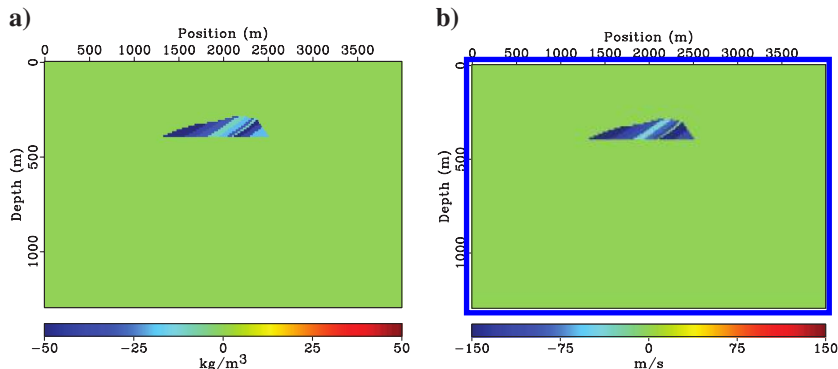


Figure 3. The true time-lapse images (difference between baseline and monitor model). (a) Density  $\rho$  and (b)  $V_p$ .

Now, assume that a migrated image  $I$  has been obtained using the above-mentioned procedure. The next step is to run a contrast estimation algorithm on  $I$ , where the image is scanned and contrasts are detected. We use a very simple approach in which  $I$  is scanned pixel by pixel, and if the difference between the current pixel and the neighboring pixels is over a given threshold value, the particular pixel is marked as a contrast pixel. Assume that  $I$  is an  $N \times M$  rectangular image. We define the local contrast function as

$$C(i, j) = \max \left( \left| \frac{|I(i, j+1) - I(i, j)|}{|I_{\max}| + |I_{\min}|} \right|, \left| \frac{|I(i+1, j) - I(i, j)|}{|I_{\max}| + |I_{\min}|} \right| \right), \quad (11)$$

where  $I(i, j)$  is the pixel value at the point  $(i, j)$ ,  $I_{\min}$  and  $I_{\max}$  are the minimum and maximum pixel value in the image, respectively. The contrast image  $R(i, j)$  is then given as

$$R(i, j) = \begin{cases} 1 & \text{if } C(i, j) \geq \beta, \\ 0 & \text{otherwise,} \end{cases} \quad (12)$$

where  $\beta$  is the threshold value. It is worth mentioning that the above algorithm can be viewed as the simplest form of an edge detection algorithm in image processing, and that other and more sophisticated contrast detection algorithms may be used to create the contrast image.

Instead of adding the contrast image as a weighting matrix on a regularization term to the objective function, we multiply the gradient of  $\Psi(\mathbf{m})$  with the matrix. This procedure will force the inversion to only make updates locally in the monitor model, and thus enhance the changes of convergence to the correct solution.

## RESULTS

To investigate different aspects of the implementation of TLFWI and LMR, we use a synthetic model inspired by the Gullfaks field in the Norwegian North Sea. The target zone is a shallow reservoir located at 400-m depth. The synthetic time-lapse effects are simulated using two versions of the model. After the sensitivity tests, we apply the methods on a real data set from the Norwegian North Sea. In between the two surveys in the real time-lapse data, one of the exploration wells were exposed to an underground leakage. As a result, gas leaked from the deep reservoir into underground formations. Thus, this is a good scenario for testing TLFWI and LMR.

### Synthetic example

The target zone in the synthetic model is a reservoir located at 400-m depth and position 1500–2500 m (Figure 2). To simulate time-lapse effects, we use two versions of the models; one where the reservoir is oil filled and one where the reservoir is water filled. The P-wave velocities

and the densities are different between the models, whereas the S-wave velocities are equal. The differences between the two models are small and shallow (Figure 3).

The synthetic data are generated using a standard finite-difference implementation of the elastic wave equation (Virieux, 1986). We simulate a marine seismic survey consisting of 275 shots. The source is located at 10-m depth. The streamer is located at 10-m depth and consists of 130 receivers with a receiver sampling of 10 m. The source signature is a Ricker wavelet with center frequency of 10 Hz. The setup is identical in the baseline and monitor survey. The numerical grid is regular with grid size 10 m, and is the same in the modeling and inversion. To simulate the nonreflecting boundaries, we use perfectly matching layer absorbing-boundary conditions (Berenger, 1994; Zhen et al., 2009). The reflecting free surface at the top of the model is implemented using the method described in Mittet (2002).

To create the initial model for the inversion, we run WEMVA with a initial model that only varies in depth (Figure 4a). The initial model is relatively far away from the true model. The final model for WEMVA (Figure 4b), which is our initial model for FWI, is a smooth model with lateral variances in the shallow part of the model. By comparing the initial and the final models, we observe that WEMVA has mainly updated the shallow parts of the model.

#### Sensitivity analysis

The sensitivity analysis of the implementation of FWI is carried out using the model for the baseline case. To investigate the behavior of our data norm, no regularization term is used in the misfit functional 1 during the analysis. In the first test, we invert for  $V_P$ , keeping  $V_S$  and  $\rho$  equal to the true models. This is somewhat a best-case scenario and is an easy way to investigate what FWI is able to recover. The final inverted  $V_P$  model is shown in Figure 5a. Residual plots for the first and last iterations for a given shot are given in Figure 6, whereas a vertical profile is given in Figure 7a.

Inverting for one parameter keeping the two others equal to the true models are not realistic. In the next test, we invert for  $V_P$  and update  $V_S$  and  $\rho$  in each iteration using the empirical relations given in equations 8 and 9, respectively. Our density and velocity models do not follow the empirical relations, so that errors are introduced in the inversion in this case. The differences between the true model and the model obtained using the empirical relations are for  $\rho$  in the range  $-183$  to  $153$  kg/m<sup>3</sup>, and for  $V_S$  in the range  $-390$  to  $0$  m/s. The largest differences for  $V_S$  are for the areas inside the reservoir.

Because the differences in the true models and the empirical models are large, we carefully check which parameter introduces the largest error during the inversion. We run the inversion

in which we only update  $\rho$  using the empirical relation and keeping  $V_S$  equal to the true model. The inverted  $V_P$  model in this case is given in Figure 5b. Now, we run the inversion with  $\rho$  equal to the true model, and  $V_S$  is updated using the empirical relation. The inverted model is given in Figure 5c. We do a final inversion where we update  $\rho$  and  $V_S$  simultaneously in the inversion. The inverted  $V_P$  model is given in Figure 5d and the vertical profile in Figure 7b.

The final test in the analysis is a comparison of elastic and acoustic inversion using elastic data. We put  $V_S$  equal to zero, and performed an inversion for  $V_P$  in which we held  $\rho$  equal to the true model. The vertical profile and the inverted model for  $V_P$  are given in Figures 7c and 8, respectively.

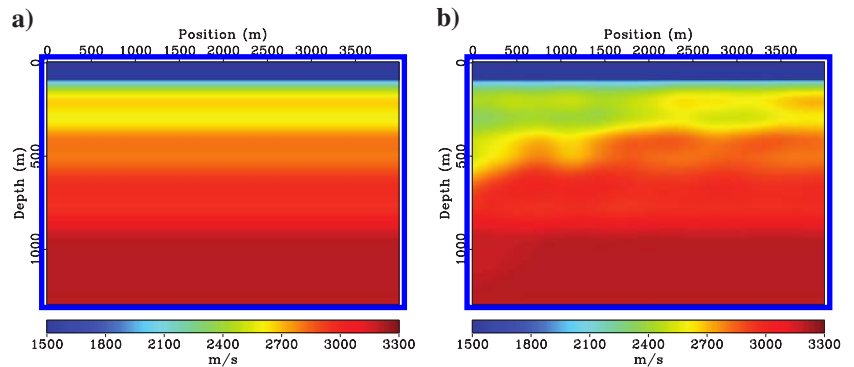


Figure 4. (a) The initial  $V_P$  model for WEMVA and (b) the initial  $V_P$  model for FWI obtained using WEMVA.

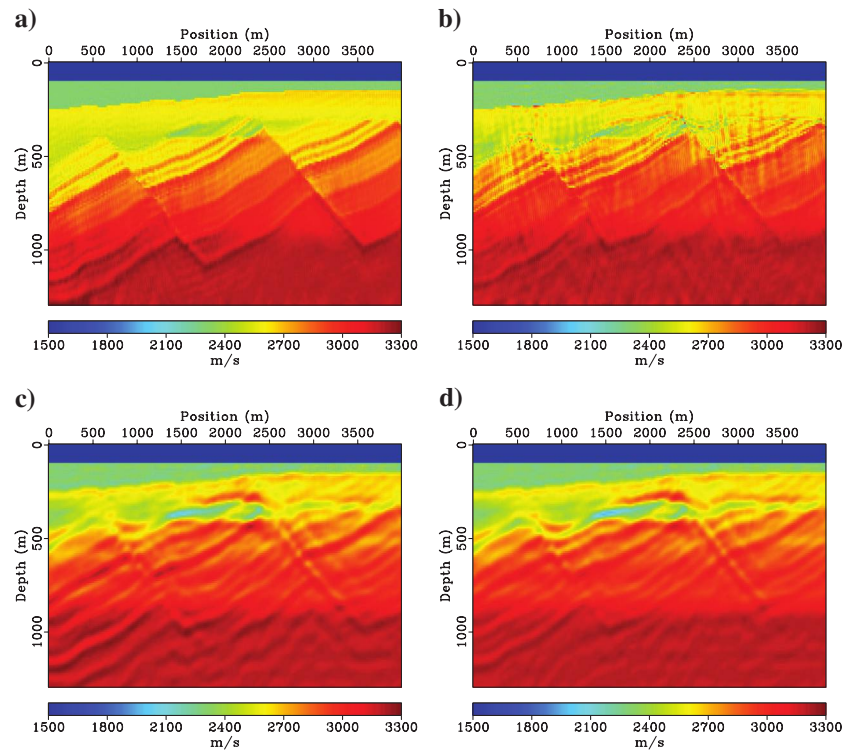


Figure 5. Inverted  $V_P$  model. (a) With  $V_S$  and  $\rho$  equal to the true models, (b) with  $V_S$  equal to the true model and  $\rho$  updated using empirical relation, (c) with  $\rho$  equal to the true model and  $V_S$  updated using empirical relation, and (d)  $V_S$  and  $\rho$  updated using empirical relations.

From this analysis, it is clear that under ideal conditions FWI is able to recover the  $V_p$  model. As information is gradually removed the inverted models start to lose resolution. However, FWI is able to recover the shallow parts of the models, whereas the deeper parts are more or less unchanged. The results for the acoustic inversion prove that the inversion fails, and the acoustic approximation is invalid in this case.

#### Time-lapse analysis

The time-lapse analysis is carried out in the same manner as the sensitivity analysis. We test the three approaches and LMR inverting for  $V_p$  using the true models for  $V_s$  and  $\rho$ , and the empirical relations given in equations 8 and 9.

The time-lapse images for  $V_p$  using approach 1 are shown in Figure 9, approach 2 in Figure 10, and approach 3 in Figure 11. The contrast image using the LMR method is shown in Figure 12. We find it inappropriate to use the sharp contrast image as a regularization for the gradient due to artifacts in the resulting time-lapse images. We therefore apply a triangle smoothing operator on the contrast image before it is applied in the inversion. The resulting time-lapse images using this method are shown in Figure 13. The time-lapse image for acoustic FWI is given in Figure 14.

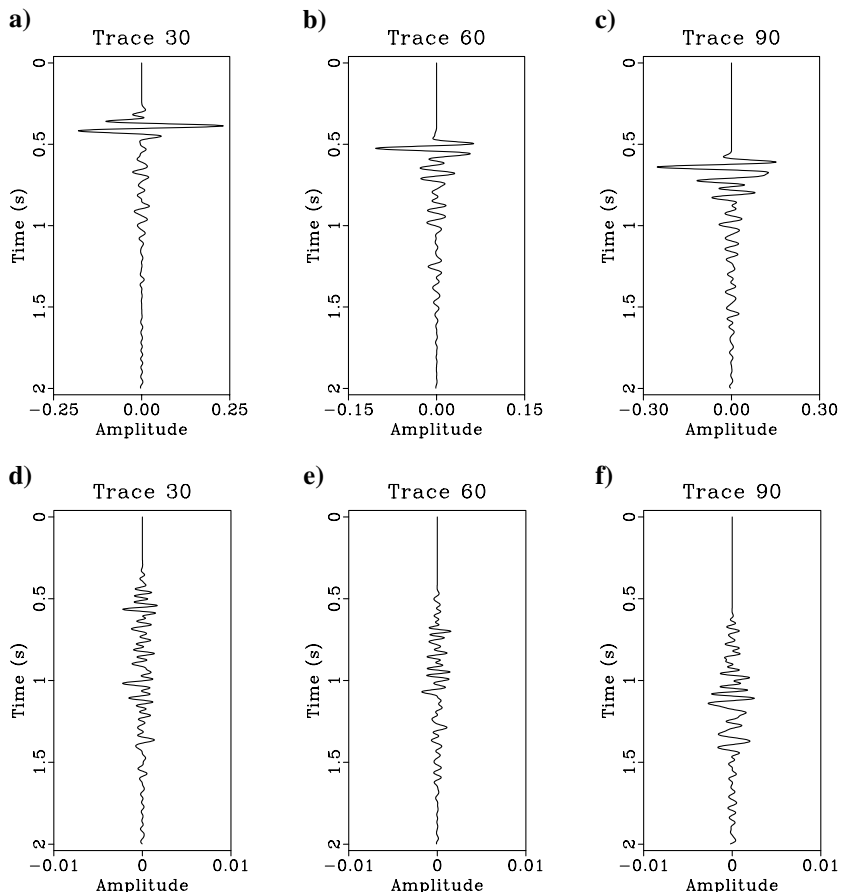


Figure 6. Trace residuals for the sensitivity analysis. (a-c) At first iteration and (d-e) at last iteration.

All elastic time-lapse images suffer from artifacts in terms of oscillations. For the cases where  $V_s$  and  $\rho$  are equal to the exact models, there are no major differences between approaches 1 and 2 in terms of artifacts. For approach 3 and LMR there are only artifacts above and below the time-lapse anomaly, and the total amount of artifacts in the images are less than with the two other approaches. For the cases where the empirical relations are used to update  $V_s$  and  $\rho$ , there are no significant differences between the images for approaches 1, 2, and 3 in terms of artifacts. The artifacts in the LMR image are visible in the areas where model updates are allowed. The acoustic inversion fails in recovering the time-lapse anomaly.

#### Real example

The real data example is from a field in the southern part of the Norwegian North Sea. In 1989, one of the exploration wells were exposed to a underground leakage. As a result, gas migrated from the deep reservoir into shallow underground formations. The underground leakage lasted for 326 days, and was stopped by a relief well. During the period of drilling the relief well, several seismic surveys were acquired for monitoring the situation. We use two data sets from the surveys; the baseline data set is a survey acquired in 1988, that is, before the blowout, and the monitor data set is from a survey in 1990, after the relief well was drilled. We refer to Landrø (2011) for a more detailed explanation of the underground blowout, and time-lapse analysis results.

Each of the two data sets consists of 460 shots. The streamer has 95 receivers with a spacing of 12.5 m. The total streamer length is 1253 m, and the shot sampling is 12.5 m. To transform the data sets from a real 3D world into our 2D numerical setting, the data sets were regularized into the same rectangular grid using linear interpolation. By comparing the two data sets using a time-shift crosscorrelation function, a static time-shift of 2 ms was found and removed. The data sets were multiplied with a square-root-of-time gain function to account for the 3D wave propagation. Both data sets suffer from several notches in the frequency spectra, so a band-pass filter with frequency band 2–20 Hz was applied. The numerical modeling is performed using a rectangular grid with grid size 6.25 m, and is the same for the modeling and inversion. The initial model is once again produced using WEMVA.

We start the inversion by estimating the source signatures. To do this, we use the FWI method where the model parameters are kept constant during the iterations, and only the source signature is updated in each iteration. The  $V_p$  model is the WEMVA model, and the  $V_s$  and  $\rho$  models are obtained using the empirical relations in equations 8 and 9, respectively. We estimate a source signature for each data set.

During the preliminary test runs, severe oscillations were present in the final inverted models. To remove the artifacts, we add the prior regularization term 3. The  $\lambda$  factor in 1 is determined

such that the ratio between the data term and the regularization term is  $10^{-3}$ .

The inverted models for the baseline data set are given in Figure 15. We observe several horizontal layers at different depths, and some dipping structures are visible at approximately 200–400 m depth and position 1750 m.

The final time-lapse images using elastic and acoustic inversions are given in Figures 16 and 17, respectively. The leaking well is placed at approximately position 2200 m in the figures. Common in all images using elastic inversion is a clear anomaly visible at

approximately 500-m depth and around the position of the well. The elastic time-lapse images using approaches 1, 2, and 3 (Figure 16a, 16b, and 16c) show repeated anomalies at position 1000 m. There are significant differences in the time-lapse images obtained using approaches 1 and 2, and the time-lapse image using approach 3. As in the synthetic case, we observe large differences between the acoustic and the elastic time-lapse images. The acoustic time-lapse image (Figure 17) shows large horizontal anomalies in depth. The sea-bottom is approximately at 70-m depth, and we observe that there are clear effects at that position in the elastic and acoustic time-lapse images.

Figure 18 shows traces from the real and inverted baseline data sets. We observe that the inversion is able to match the true baseline data set. In Figure 19 residual traces between the baseline and monitor data sets for the real and inverted data sets are shown. We observe that the events are correctly placed in time, but that the amplitudes between the real and inverted residuals differ.

## DISCUSSION

The synthetic tests show that FWI is able to recover the model parameters, and reveal time-lapse changes in the velocity models. Artifacts from the inversions are visible in all time-lapse images for

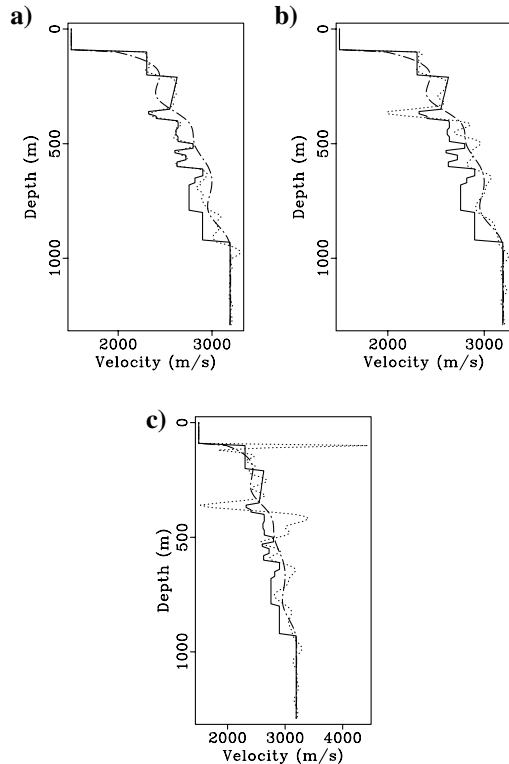


Figure 7. Vertical profiles of the  $V_p$  model (true model: solid line, initial model: dot-and-dashed line, the inverted model: dotted line). (a) Here,  $\rho$  and  $V_S$  known, (b) empirical relations, and (c) acoustic inversion.

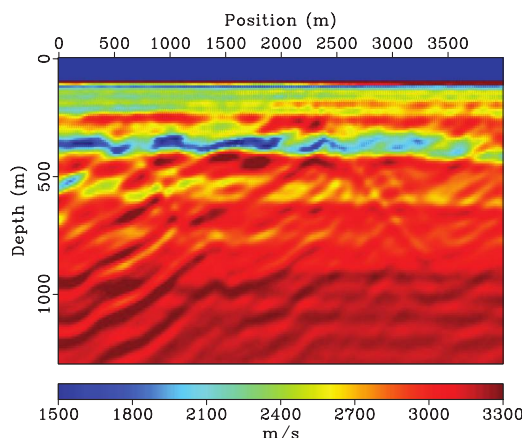


Figure 8. Acoustic FWI with  $\rho$  equal to the true model.

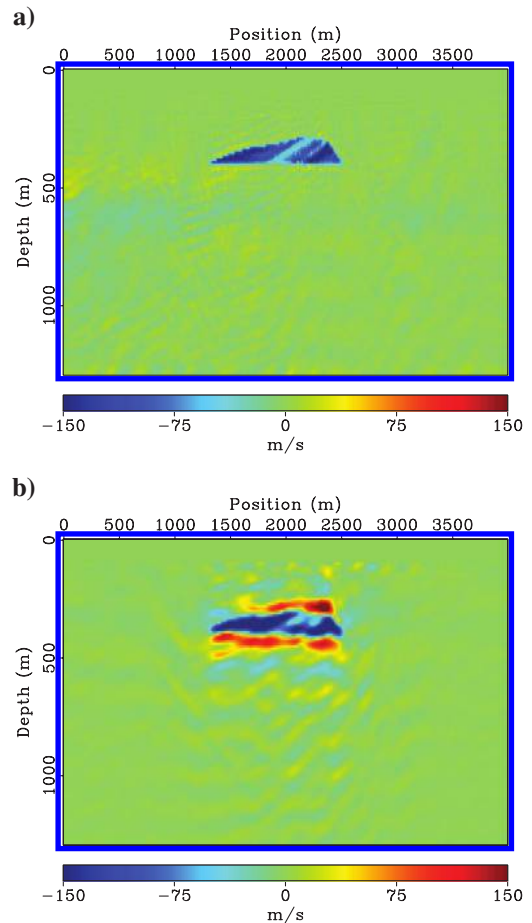


Figure 9. Time-lapse images for  $V_p$  using approach 1. (a) When  $V_S$  and  $\rho$  are equal to the true models and (b) when empirical relations are used to update  $V_S$  and  $\rho$ .

the different approaches tested. As a consequence of the model update constraint in LMR, the images using LMR contain only artifacts in the areas where the models are allowed to be updated.

The FWI is a highly ill-posed problem, and inverting for all three model parameters at the same time is hard to accomplish. To be more precise; in our synthetic and real examples, the only parameter we were able to invert for using FWI was the P-wave velocity model. A way to get estimates for the two other parameters is to use empirical relations to link the inverted parameter with the two other parameters. This produces the best results when we only invert for one parameter. On the other hand, empirical relations should be used with extreme care because they are valid for restricted rock types, and they may introduce spurious structures in the subsurface, which in some cases may be problematic. We believe, however, that it is better to update the two parameters during the inversion, than keeping them constant during the iterations, as long as the empirical relations are relatively close to true models.

Our synthetic models do not follow the empirical relations we use in the inversion. From the sensitivity analysis (Figure 5) it is clear that it is important to use empirical relations that are close to the true models. The relation for the density gives models that are relatively close to the solution, whereas the relation for the S-wave velocity gives models that are far away from the true model. The inversion results using the S-wave relation (Figure 5c and 5d),

are mainly a consequence of the fact that the empirical relation is not able to predict the correct S-wave velocities inside the reservoir. The empirical S-wave relation has introduced a spurious structure in the subsurface, and the consequences of this fake structure on the time-lapse images are large (Figures 9–11 and 13). The time-lapse artifacts are large when empirical relations are used without any kind of regularization or model constraint.

With this in mind, one can question the validity of the empirical relations used to update the density and S-wave velocity models for the real example. The choice of empirical relations was based on knowledge of the rock types from the area that the example is taken from. The density relation 9 is valid for many rock types (Gardner et al., 1974), whereas the S-wave relation 8 is valid mainly for mud-rocks (Castagna et al., 1985). We therefore believe that our choice of empirical relations is relatively close to the real models. Of course, our results should be interpreted with caution because the empirical relations are not a perfect match of the truth.

The failure of the acoustic inversion (Figures 8, 14, and 17) is somewhat of a surprise. The major difference between acoustic and elastic data, is the amplitudes of the events in the data due to the differences in the reflection and transmission coefficients. From this, it is obvious what happens during the acoustic inversion. To match the amplitudes, the inversion updates the velocity model too much (Figure 7c). The acoustic time-lapse image for the real

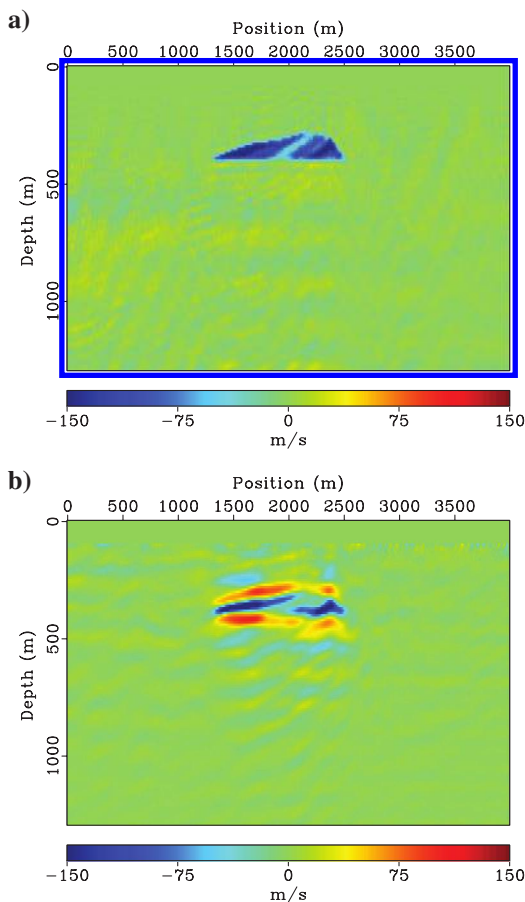


Figure 10. Time-lapse images for  $V_p$  using approach 2. (a) When  $V_s$  and  $\rho$  are equal to the true models and (b) when empirical relations are used to update  $V_s$  and  $\rho$ .

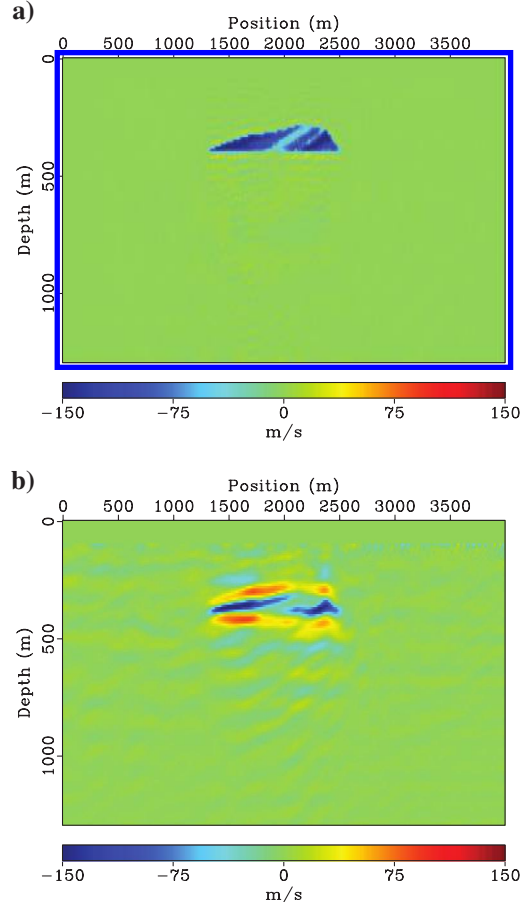


Figure 11. Time-lapse images for  $V_p$  using approach 3. (a) When  $V_s$  and  $\rho$  are equal to the true models and (b) when empirical relations are used to update  $V_s$  and  $\rho$ .

example (Figure 17) shows several horizontal time-lapse effects, which obviously is not correct. The results show that elastic theory is important for the success of FWI using data that primarily consist of reflected events and support the findings of Barnes and Charara (2009).

The LMR approach is an idea for removing most of the artifacts, by only allowing the monitor model update for certain parts of the model. The time-lapse image, using empirical relations and LMR (Figure 13b), manages to reveal the shape of the anomaly satisfactorily, still with artifacts above and below the anomaly. It turns out that the success of LMR is dependent on the migration method, the models, and the contrast detection method used. If the contrast image is too strict, important anomalies may be overlooked in the time-lapse images. On the other hand, such a constraint may result in better focusing of the major events in the data sets. An improvement of the approach is to use a more intelligent contrast detection algorithm, which works on the whole image, and not on a pixel-by-pixel basis. Though not formally correct mathematically, changing the gradient gives better convergence of the inverse method, and thus better time-lapse images.

The conversion of the real data sets from 3D to 2D, may influence the inversion results (Auer et al., 2013). The inversions may introduce spurious results that overwhelm subtle changes sought during time-lapse inversion. Moreover, the two data sets may include different time-dependent error sources, which FWI will explain by changing the models differently in the inversions. Such discrepancies may have impact on the final time-lapse images.

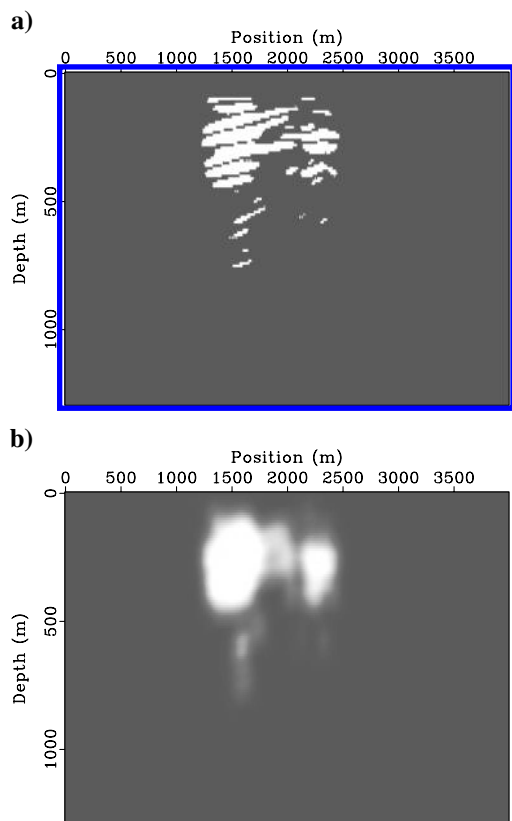


Figure 12. Contrast images created using the LMR method. (a) Before smoothing and (b) after smoothing.

The success of FWI is dependent on the source function used in the inversions. For the real example, we estimated source signatures for each of the data sets using FWI, and used the same source signature for all the shots in each data set. In an inversion setup, this

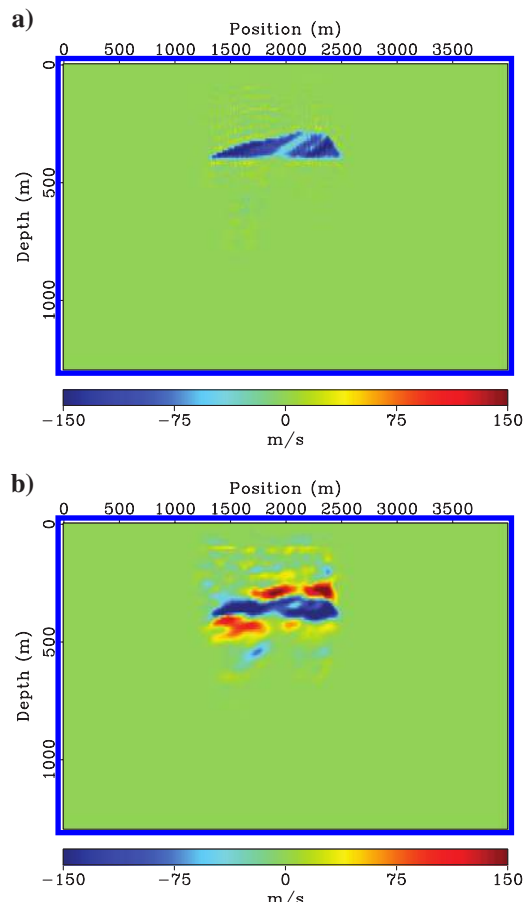


Figure 13. Time-lapse images for  $V_p$  using approach 2 and LMR. (a) When  $V_s$  and  $\rho$  are equal to the true models and (b) when empirical relations are used to update  $V_s$  and  $\rho$ .

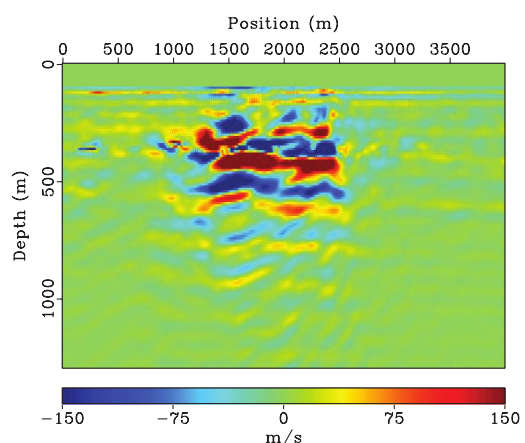


Figure 14. Acoustic time-lapse image with  $\rho$  equal to the true model.

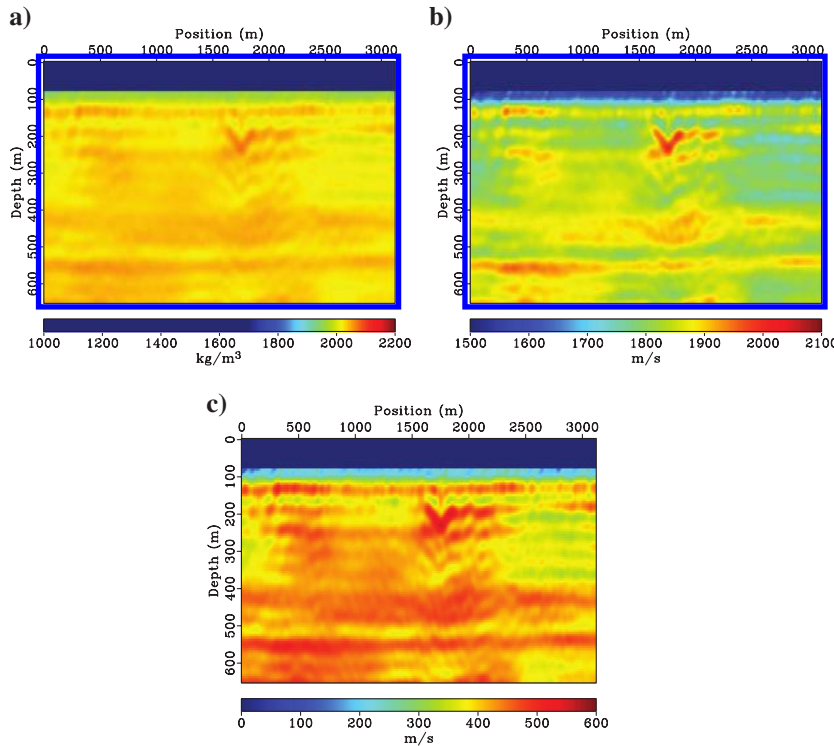


Figure 15. Inverted models for the baseline data set for the real example. (a) Density  $\rho$ , (b)  $V_p$ , and (c)  $V_s$ .

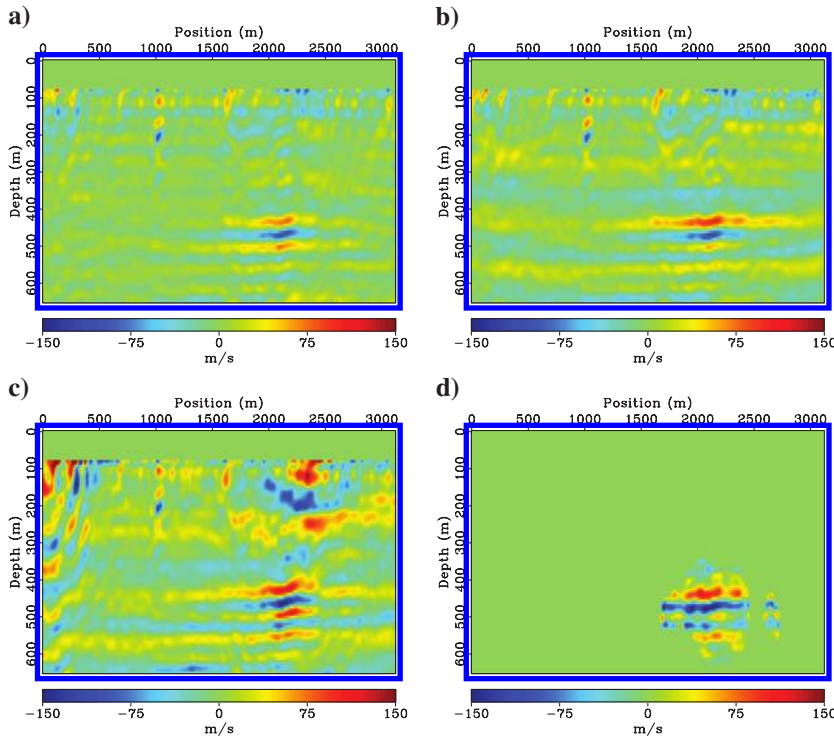


Figure 16. Time-lapse images for  $V_p$  for the real example. (a) Approach 1, (b) approach 2, (c) approach 3, and (d) LMR.

may be too strict an assumption, even though the repeatability of the air gun signatures are considered good. An alternative, is to estimate the source signature in each shot using our approach. Another alternative is to use the method described by Maurer et al. (2012), where one in addition to the source signatures solve for source-receiver coupling effects.

The results for the real example should be interpreted with all the above-mentioned uncertainties in mind.

The comparison of the real and synthetic data sets (Figures 18 and 19) shows that the inversion is able to produce synthetic data that are close to the real data. The major differences between the real and the inverted data sets are in the residuals between the baseline and monitor data sets. The difference can be explained by the fact that the real experiment is a 3D problem, which we have approximated using a 2D approach in the inversion. Another explanation is that the inversions are focused on minimizing the residuals of the data set itself, and not the residual between the data sets.

The time-lapse images for the real leakage well (Figure 16) show several interesting anomalies. The largest common anomaly in all images is located at approximately 500-m depth. There is a sand layer at 490-m depth and smaller sand layers at 523- and 562-m depth (Landrø, 2011). During the leakage, gas migrated into the sand layer at 490-m depth, and there could be gas inside the small sand layers at the deeper depths (Landrø, 2011). Gas in the sand layer should result in a decrease in P-wave velocity in this area. On the time-lapse images a decrease in P-wave velocity in this area is clearly visible. Above and below the negative time-lapse anomaly, positive anomalies are visible. We believe that the positive anomalies are a consequence of the limited-offset and the low frequencies in the real data sets, and thus are artifacts from the inversions. On the images using approach 3 and LMR (Figure 16c and 16d), a second negative anomaly is visible at approximately 525-m depth. This anomaly may be the result of gas in the sand layer at 523-m depth, or it could be an artifact from the anomaly at 500-m depth.

The relief well was drilled at a distance of 1.2 km from the leaking well. It is interesting that some repeated anomalies are visible at the 1000-m position (Figure 16a, 16b, and 16c), which is close to the position where the relief well is located in the image. It is a surprise that this well seems to be visible in the time-lapse images. The relief well was drilled on the edge of the area that was filled with leaked gas. Thus, gas may have migrated along the walls of the well, or the well itself produced seismic differences that give the time-lapse response.

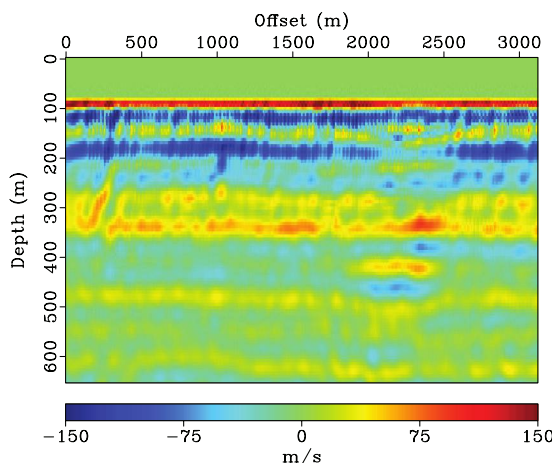


Figure 17. Time-lapse image for  $V_p$  for the real example using acoustic inversion and approach 1.

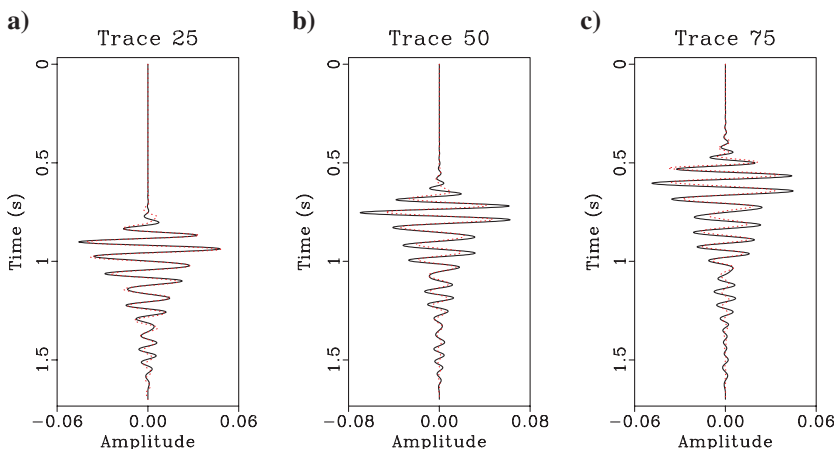


Figure 18. Traces from the real baseline data set (solid lines) and the inverted baseline data set (dotted lines).

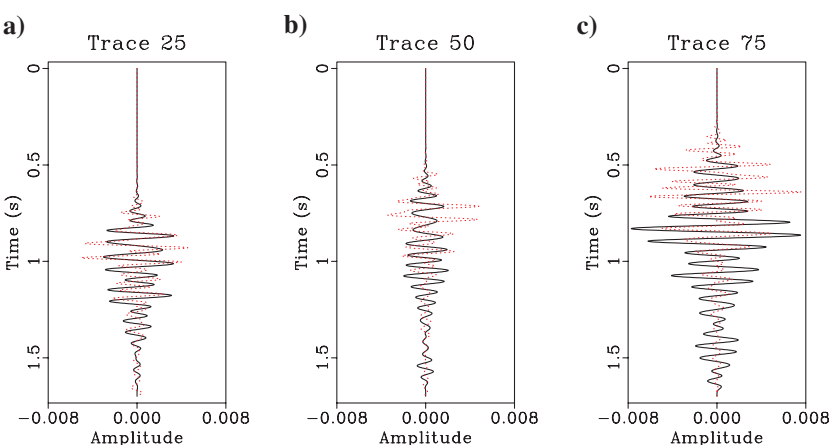


Figure 19. Residual traces between the baseline and monitor data sets for the real data sets (solid lines), and the inverted data sets (dotted lines).

There is a significant difference between the time-lapse image for approach 3 and the other time-lapse images. The two data sets were not acquired with time-lapse imaging in mind, and as a result the repeatability in the data sets is not as good as it may have been. The residual between the baseline and monitor data sets, which is used to create the new monitor data set for approach 3, is influenced by this fact. We believe the anomalies on the left and in the upper parts in the image are time-lapse artifacts introduced by the monitor inversion to explain the differences due to the repeatability issue.

## CONCLUSION

We have used FWI on synthetic and real limited-offset time-lapse data sets. The synthetic and real tests show that elastic theory is necessary for the success of FWI when seismic data primarily consisting of reflected events are used. We have introduced an LMR method, whose purpose is to reduce time-lapse artifacts. This method, in addition to three other approaches for creating time-lapse images using FWI, have been tested. All approaches are able to reveal time-lapse changes, though with small differences. The LMR approach is able to remove time-lapse artifacts by allowing only the updates to be performed in specific parts of the model.

## ACKNOWLEDGMENTS

This work has been produced with support from the BIGCCS Centre, and performed under the Norwegian research program Centres for Environment-Friendly Energy Research (FME). The authors acknowledge the following partners for their contributions: ConocoPhillips, Gassco, Shell, Statoil, TOTAL, GDF SUEZ, and the Research Council of Norway (193816/S60). We thank W. Weibull for creating the initial models for FWI and for fruitful comments on the manuscript. We also thank the ROSE Consortium and their sponsors for support.

## REFERENCES

- Auer, L., A. Nuber, S. Greenhalgh, H. Maurer, and S. Marelli, 2013, A critical appraisal of asymptotic 3D-to-2D data transformation in full-waveform seismic crosshole tomography: *Geophysics*, **78**, no. 6, R235–R247, doi: [10.1190/geo2012-0382.1](https://doi.org/10.1190/geo2012-0382.1).
- Barnes, C., and M. Charara, 2009, The domain of applicability of acoustic full-waveform inversion for marine seismic data: *Geophysics*, **74**, no. 6, WCC91–WCC103, doi: [10.1190/1.3250269](https://doi.org/10.1190/1.3250269).
- Berenger, J.-P., 1994, A perfectly matched layer for the absorption of electromagnetic waves: *Journal of Computational Physics*, **114**, 185–200, doi: [10.1006/jcph.1994.1159](https://doi.org/10.1006/jcph.1994.1159).
- Brossier, R., S. Operto, and J. Virieux, 2009, Seismic imaging of complex onshore structures by 2D elastic frequency-domain full-waveform inversion: *Geophysics*, **74**, no. 6, WCC105–WCC118, doi: [10.1190/1.3215771](https://doi.org/10.1190/1.3215771).
- Castagna, J., M. Batzle, and R. Eastwood, 1985, Relationships between compressional-wave and shear-wave velocities in clastic silicate rocks: *Geophysics*, **50**, 571–581, doi: [10.1190/1.1441933](https://doi.org/10.1190/1.1441933).

- Choi, Y., and T. Alkhalifah, 2012, Application of multi-source waveform inversion to marine streamer data using the global correlation norm: *Geophysical Prospecting*, **60**, 748–758, doi: [10.1111/j.1365-2478.2012.01079.x](https://doi.org/10.1111/j.1365-2478.2012.01079.x).
- Gardner, G., L. Gardner, and A. Gregory, 1974, Formation velocity and density — The diagnostics basics for stratigraphic traps: *Geophysics*, **39**, 770–780, doi: [10.1190/1.1440465](https://doi.org/10.1190/1.1440465).
- Greaves, R., and T. Fulp, 1987, Three-dimensional seismic monitoring of an enhanced oil recovery process: *Geophysics*, **52**, 1175–1187, doi: [10.1190/1.1442381](https://doi.org/10.1190/1.1442381).
- Landro, M., 2011, Seismic monitoring of an old underground blowout — 20 years later: *First Break*, **29**, 39–48, doi: [10.3997/1365-2397.2011017](https://doi.org/10.3997/1365-2397.2011017).
- Landro, M., O. A. Solheim, E. Hilde, B. O. Ekren, and L. K. Strønen, 1999, The Gullfaks 4D seismic study: *Petroleum Geoscience*, **5**, 213–226, doi: [10.1144/petgeo.5.3.213](https://doi.org/10.1144/petgeo.5.3.213).
- Lumley, D., D. C. Adams, M. Meadows, S. Cole, and R. Wright, 2003, 4D seismic data processing issues and examples: 73rd Annual International Meeting, SEG, Expanded Abstracts, 1394–1397.
- Maurer, H., S. Greenhalgh, E. Manukyan, S. Marelli, and A. Green, 2012, Receiver-coupling effects in seismic waveform inversions: *Geophysics*, **77**, no. 1, R57–R63, doi: [10.1190/geo2010-0402.1](https://doi.org/10.1190/geo2010-0402.1).
- Mittet, R., 2002, Free-surface boundary conditions for elastic staggered-grid modeling schemes: *Geophysics*, **67**, 1616–1623, doi: [10.1190/1.1512752](https://doi.org/10.1190/1.1512752).
- Mora, P., 1987, Nonlinear two-dimensional elastic inversion of multioffset seismic data: *Geophysics*, **52**, 1211–1228, doi: [10.1190/1.1442384](https://doi.org/10.1190/1.1442384).
- Nocedal, J., and S. J. Wright, 2006, Numerical optimization, 2nd ed.: Springer Science + Business Media, LLC.
- Queißer, M., and S. Singh, 2010, Time lapse seismic monitoring of CO<sub>2</sub> sequestration at Sleipner using time domain 2D full waveform inversion: 80th Annual International Meeting, SEG, Expanded Abstracts, 2875–2879.
- Raknes, E. B., W. Weibull, and B. Arntsen, 2013, Time-lapse full waveform inversion: Synthetic and real data examples: 83rd Annual International Meeting, SEG, Expanded Abstracts, 1–4.
- Routh, P., G. Palacharla, I. Chikichev, and S. Lazaratos, 2012, Full wavefield inversion of time-lapse data for improved imaging and reservoir characterization: 82nd Annual International Meeting, SEG, Expanded Abstracts, 1–6.
- Scales, J. A., P. Docherty, and A. Gerszenkorn, 1990, Regularisation of nonlinear inverse problems: Imaging the near-surface weathering layer: *Inverse Problems*, **6**, 115–131, doi: [10.1088/0266-5611/6/1/011](https://doi.org/10.1088/0266-5611/6/1/011).
- Shipp, R. M., and S. C. Singh, 2002, Two-dimensional full wavefield inversion of wide-aperture marine seismic streamer data: *Geophysical Journal International*, **151**, 325–344, doi: [10.1046/j.1365-246X.2002.01645.x](https://doi.org/10.1046/j.1365-246X.2002.01645.x).
- Tarantola, A., 1984, Inversion of seismic reflection data in the acoustic approximation: *Geophysics*, **49**, 1259–1266, doi: [10.1190/1.1441754](https://doi.org/10.1190/1.1441754).
- Virieux, J., 1986, P-SV wave propagation in heterogeneous media: Velocity-stress finite-difference method: *Geophysics*, **51**, 889–901, doi: [10.1190/1.1442147](https://doi.org/10.1190/1.1442147).
- Virieux, J., and S. Operto, 2009, An overview of full-waveform inversion in exploration geophysics: *Geophysics*, **74**, no. 6, WCC1–WCC26, doi: [10.1190/1.3238367](https://doi.org/10.1190/1.3238367).
- Weibull, W., B. Arntsen, and E. Nilsen, 2012, Initial velocity models for full waveform inversion: 82nd Annual International Meeting, SEG, Expanded Abstracts, 1–4.
- Zhang, F., C. Juhlin, M. Ivandic, and S. Lüth, 2013, Application of seismic full waveform inversion to monitor CO<sub>2</sub> injection: Modelling and a real data example from the Ketzin site, Germany: *Geophysical Prospecting*, **61**, 284–299, doi: [10.1111/1365-2478.12021](https://doi.org/10.1111/1365-2478.12021).
- Zhen, Q., L. Minghui, Z. Xiaodong, Y. Yao, Z. Cai, and S. Jianyong, 2009, The implementation of an improved NPML absorbing boundary condition in elastic wave modeling: *Applied Geophysics*, **6**, 113–121, doi: [10.1007/s11770-009-0012-3](https://doi.org/10.1007/s11770-009-0012-3).
- Zheng, Y., P. Barton, and S. Singh, 2011, Strategies for elastic full waveform inversion of time-lapse ocean bottom cable (OBC) seismic data: 81st Annual International Meeting, SEG, Expanded Abstracts, 4195–4200.

This article has been cited by:

1. Di Yang, Mark Meadows, Phil Inderwiesen, Jorge Landa, Alison Malcolm, Michael Fehler. 2015. Double-difference waveform inversion: Feasibility and robustness study with pressure data. *GEOPHYSICS* 80:6, M129–M141. [[Abstract](#)] [[Full Text](#)] [[PDF](#)] [[PDF w/Links](#)]
2. Espen Birger Raknes, Børge Arntsen. 2015. A numerical study of 3D elastic time-lapse full-waveform inversion using multicomponent seismic data. *GEOPHYSICS* 80:6, R303–R315. [[Abstract](#)] [[Full Text](#)] [[PDF](#)] [[PDF w/Links](#)]
3. Espen Birger Raknes, Wiktor Weibull, Børge Arntsen. 2015. Seismic imaging of the carbon dioxide gas cloud at Sleipner using 3D elastic time-lapse full waveform inversion. *International Journal of Greenhouse Gas Control* 42, 26–45. [[CrossRef](#)]
4. Tore S. Bergslid\*, Espen Birger Raknes, Børge ArntsenThe influence of anisotropy on elastic full-waveform inversion 1425-1429. [[Abstract](#)] [[References](#)] [[PDF](#)] [[PDF w/Links](#)]
5. Espen Birger Raknes, Børge Arntsen, Wiktor Weibull. 2015. Three-dimensional elastic full waveform inversion using seismic data from the Sleipner area. *Geophysical Journal International* 202:3, 1877. [[CrossRef](#)]
6. Espen Birger Raknes, Wiktor Weibull, Børge Arntsen. 2014. Elastic velocity analysis and time-lapse full-waveform inversion. *The Leading Edge* 33:9, 1000-1006. [[Abstract](#)] [[Full Text](#)] [[PDF](#)] [[PDF w/Links](#)]
7. Espen Birger Raknes\*, Børge Arntsen3D elastic time-lapse full waveform inversion using multi-component seismic data 1939-1944. [[Abstract](#)] [[References](#)] [[PDF](#)] [[PDF w/Links](#)]